SN 2023ixf in Messier 101: A Variable Red Supergiant as the Progenitor Candidate to a Type II Supernova

Charles D. Kilpatrick[1] , Ryan J. Foley[2] , Wynn V. Jacobson-Galán[3] , Anthony L. Piro[4] , Stephen J. Smartt[5,6] ,
Maria R. Drout[7] , Alexander Gagliano[8,9,18] , Christa Gall[10] , Jens Hjorth[10] , David O. Jones[11] , Kaisey S. Mandel[12] ,
Raffaella Margutti[3] , Enrico Ramirez-Ruiz[2] , Conor L. Ransome[13] , V. Ashley Villar[13,14,15] , David A. Coulter[2] ,
Hua Gao[16] , David Jacob Matthews[3] , Kirsty Taggart[2] , and Yossef Zenati[17,19]

[1] Center for Interdisciplinary Exploration and Research in Astrophysics (CIERA) and Department of Physics and Astronomy, Northwestern University, Evanston, IL 60208, USA; ckilpatrick@northwestern.edu
[2] Department of Astronomy and Astrophysics, University of California, Santa Cruz, CA 95064, USA
[3] Department of Astronomy and Astrophysics, University of California, Berkeley, CA 94720, USA
[4] The Observatories of the Carnegie Institution for Science, 813 Santa Barbara St., Pasadena, CA 91101, USA
[5] Astrophysics Research Centre, School of Mathematics and Physics, Queen's University Belfast, Belfast BT7 1NN, UK
[6] Department of Physics, University of Oxford, Denys Wilkinson Building, Keble Road, Oxford OX1 3RH, UK
[7] David A. Dunlap Department of Astronomy and Astrophysics, University of Toronto, 50 St. George Street, Toronto, Ontario M5S 3H4 Canada
[8] Department of Astronomy, University of Illinois at Urbana-Champaign, 1002 W. Green St., IL 61801, USA
[9] Center for Astrophysical Surveys, National Center for Supercomputing Applications, Urbana, IL 61801, USA
[10] DARK, Niels Bohr Institute, University of Copenhagen, Jagtvej 128, DK-2200 Copenhagen, Denmark
[11] Gemini Observatory, NSF's NOIRLab, 670 N. A'ohoku Place, Hilo, HI 96720, USA
[12] Institute of Astronomy and Kavli Institute for Cosmology, Madingley Road, Cambridge CB3 0HA, UK
[13] Department of Astronomy and Astrophysics, The Pennsylvania State University, Davey Lab, State College, PA 16802, USA
[14] Institute for Computational & Data Sciences, The Pennsylvania State University, University Park, PA 16802, USA
[15] Institute for Gravitation and the Cosmos, The Pennsylvania State University, University Park, PA 16802, USA
[16] Institute for Astronomy, University of Hawaii, 2680 Woodlawn Drive, Honolulu, HI 96822, USA
[17] Department of Physics and Astronomy, The Johns Hopkins University, Baltimore, MD 21218, USA; ckilpatrick@northwestern.edu

Abstract

We present preexplosion optical and infrared (IR) imaging at the site of the type II supernova (SN II) 2023ixf in Messier 101 at 6.9 Mpc. We astrometrically registered a ground-based image of SN 2023ixf to archival Hubble Space Telescope (HST), Spitzer Space Telescope (Spitzer), and ground-based near-IR images. A single point source is detected at a position consistent with the SN at wavelengths ranging from HST R band to Spitzer 4.5 μm. Fitting with blackbody and red supergiant (RSG) spectral energy distributions (SEDs), we find that the source is anomalously cool with a significant mid-IR excess. We interpret this SED as reprocessed emission in a 8600 $R_{\odot}$ circumstellar shell of dusty material with a mass $\sim 5 \times 10^{-5} M_{\odot}$ surrounding a $\log(L/L_{\odot}) = 4.74 \pm 0.07$ and $T_{\rm eff} = 3920^{+200}_{-160}$ K RSG. This luminosity is consistent with RSG models of initial mass 11 $M_{\odot}$, depending on assumptions of rotation and overshooting. In addition, the counterpart was significantly variable in preexplosion Spitzer 3.6 and 4.5 μm imaging, exhibiting $\sim 70\%$ variability in both bands correlated across 9 yr and 29 epochs of imaging. The variations appear to have a timescale of 2.8 yr, which is consistent with κ-mechanism pulsations observed in RSGs, albeit with a much larger amplitude than RSGs such as α Orionis (Betelgeuse).

1. Introduction

All hydrogen-rich supernovae (SN II) with directly identified progenitor stars have been interpreted to come from systems with initial mass $<20 M_{\odot}$ (Smartt 2015). With the exception of the blue supergiant progenitor of the peculiar SN II 1987A (Hillebrandt et al. 1987; Arnett et al. 1989), the yellow supergiant progenitor stars of hydrogen-poor SNe IIb (e.g., Aldering et al. 1994), and the luminous blue variable (LBV) progenitor stars to SNe IIn (e.g., Gal-Yam & Leonard 2009), all of these systems are red supergiants (RSGs). These stars have massive, extended, hydrogen envelopes and make up the majority of directly identified progenitor stars to core-collapse SNe (SNe 2003gd, 2004A, 2004et, 2005cs, 2006my, 2008bk, 2009hd, 2009kr, 2009md, 2012A, 2012aw, 2012ec, 2016cok, 2017eaw, 2018aoq, 2020jfo, and 2022acko; Smartt et al. 2004; Maund & Smartt 2009; Elias-Rosa et al. 2010; Fraser et al. 2010; Crockett et al. 2011; Fraser et al. 2011; Kochanek et al. 2012; Maund et al. 2013; Tomasella et al. 2013; Fraser et al. 2014; Maund et al. 2014; Kochanek et al. 2017; Kilpatrick & Foley 2018; O'Neill et al. 2019; Rui et al. 2019; Van Dyk et al. 2019; Sollerman et al. 2021; Van Dyk et al. 2023a, 2023b). The lack of $>20 M_{\odot}$ RSG progenitor stars of SNe II despite the fact that they make up $\approx 15\%$ of RSGs following a Salpeter initial mass function and RSGs with $\log(L/L_{\odot}) > 5.2$ are observed in the LMC, M31, and M33 (Drout et al. 2012; Neugent et al. 2020; Neugent 2021a, 2021b) has been noted as the "RSG problem" (Smartt et al. 2009; Smartt 2009, although see also Davies & Beasor 2018).

---

[18] NSF Graduate Research Fellow.
[19] ISEF International Fellowship.

Theoretically, massive RSGs are predicted to have compact oxygen cores, and many of them may collapse directly to black holes as "failed SNe," leading to a paucity of high-mass counterparts to SNe II (Sukhbold et al. 2016). This scenario broadly agrees with the light curves and nucleosynthetic yields of SNe II, which also favor lower-mass progenitor stars (Brown et al. 2013; Müller et al. 2017; Morozova et al. 2018) as well as direct evidence for a high-mass RSG in NGC 6946 whose optical counterpart disappeared (Adams et al. 2017; see also Neustadt et al. 2021a and Byrne & Fraser 2022). This source also left behind a weak infrared (IR) transient consistent with expectations for mass ejection in failed SNe (Lovegrove & Woosley 2013; Piro 2013; Fernández et al. 2018). Long time baseline follow up of nearby galaxies with deep, high-resolution imaging can constrain the fraction of disappearing stars, such as the estimate by the "Survey for Nothing" that $\approx 16\%$ of massive stars produce failed SNe in Neustadt et al. (2021b), close to the value required by an upper mass threshold for successful explosions of $>20\,M_\odot$ stars. Simultaneously constraining the fractions and mass distributions of failed SNe and SN II progenitor stars is therefore a powerful tool for probing massive star structure and the latest stages of stellar evolution.

SN II progenitor stars also exhibit a wide range of circumstellar densities in their immediate vicinity ($<10^{15}$ cm) as implied by flash spectroscopy (Gal-Yam et al. 2014; Khazov et al. 2016; Yaron et al. 2017; Terreran et al. 2022; Tinyanont et al. 2022), early photometric evolution (Morozova et al. 2017, 2018), as well as evidence for preexplosion variability and eruptions (Kilpatrick & Foley 2018; Jacobson-Galán et al. 2022). These features may have significant implications for the interpretation of their preexplosion counterparts in the absence of multiband, multiepoch imaging. For example, the vast majority of SN II preexplosion counterparts are identified in F814W imaging from the Hubble Space Telescope (HST; e.g., Smartt 2009; Davies & Beasor 2018). This filter is blueward of the peak of RSG spectral energy distributions (SEDs) and may be significantly impacted by circumstellar extinction in the presence of a dusty shell. Moreover, many RSGs exhibit well-known modes of variability (Stothers 1969; Jurcevic et al. 2000; Guo & Li 2002; Yang & Jiang 2011; Soraisam et al. 2018) that may become even more extreme as they approach core collapse (Yoon & Cantiello 2010; Fuller 2017; Davies et al. 2022), although SN 2016cok is a counterexample whose progenitor star exhibited very little variability (Kochanek et al. 2017). Without multiepoch imaging in which their average luminosities can be estimated, interpretation of photometry for SN II preexplosion counterparts is complicated by large systematic uncertainties.

Here we present preexplosion imaging to the nearby SN II 2023ixf discovered in Messier 101 (M101) on 2023 May 19 (Itagaki 2023). These data cover ultraviolet to mid-IR bands from 1999–2019. We demonstrate that there is a single credible progenitor candidate to SN 2023ixf and estimate its luminosity, temperature, and initial stellar mass as well as its variability and total circumstellar material (CSM) inferred from a significant mid-IR excess. We find it was significantly variable in the mid-IR and compare that timescale with well-observed RSGs. We summarize the total data set and our reduction procedure in Section 2 and the analysis and modeling of those data in Section 3. Finally, we discuss the broader implications of this progenitor candidate in Section 4 and conclude in Section 5.

Table 1
HST Photometry of the SN 2023ixf Progenitor Candidate

MJD	Instrument	Filter	m (mag)	σ_m (mag)
51260.9786	WFPC2	F656N	>23.433	⋯
51261.0390	WFPC2	F675W	26.422	0.230
51261.1120	WFPC2	F547M	>26.273	⋯
51345.9897	WFPC2	F656N	>23.776	⋯
51346.0529	WFPC2	F547M	>26.416	⋯
52593.9933	ACS/WFC	F435W	>27.393	⋯
52594.0096	ACS/WFC	F555W	>27.099	⋯
52594.0215	ACS/WFC	F814W	24.881	0.059
52878.3224	WFPC2	F336W	>27.025	⋯
53045.0069	ACS/WFC	F658N	25.332	0.284
56735.8571	WFC3/UVIS	F673N	>24.629	⋯
58207.4384	ACS/WFC	F658N	>25.488	⋯
58207.4561	ACS/WFC	F435W	>27.799	⋯

Note. All magnitudes are in the AB system.

(This table is available in machine-readable form.)

We assume a line-of-sight extinction through the Milky Way of $A_V = 0.025$ mag (assuming $R_V = 3.1$, this is $E(B - V) = 0.008$ mag) from Schlafly & Finkbeiner (2011). We also adopt the latest Cepheid distance to M101 of 6.85 ± 0.15 Mpc from Riess et al. (2022). Finally, throughout this paper we reference W. V. Jacobson-Galán et al. (2023, in preparation), who demonstrate that SN 2023ixf appears to be a normal type II SN with broad lines of hydrogen. We also assume a host reddening to SN 2023ixf of $E(B - V) = 0.033$ mag from W. V. Jacobson-Galán et al. (2023, in preparation), derived from Na I D line absorption in optical spectra of this event. Given the small value for this line-of-sight reddening, it does not significantly impact our results and we adopt a total-to-selective extinction ratio in the host galaxy of $R_V = 3.1$ (implying $A_V = 0.10$ mag), however we acknowledge that this could range from $R_V = 2$–6 (implying $A_V = 0.07$–0.20 mag).

## 2. Observations of SN 2023ifx and Its Progenitor Candidate

2.1. HST

The site of SN 2023ixf was observed with HST's WFPC2, Advanced Camera for Surveys (ACS), and WFC3 over seven epochs from 1999 March 23 to 2018 March 30, or 24.2 to 5.1 yr before discovery (Table 1). Following methods described in Kilpatrick et al. (2022) and Kilpatrick et al. (2021), we used the custom python-based pipeline hst123[20] to download, align, and drizzle all HST imaging (for details, see Hack et al. 2021), and perform photometry in dolphot (Dolphin 2016). We used recommended dolphot settings for each imager as described in the respective manual.[21]

The final stacked imaging of M101 observed in 2002 by ACS is shown in Figure 1 as an RGB image (F814W, F555W, and F435W). We also show each image in which we obtain a detection of a counterpart at the explosion site of SN 2023ixf, which includes WFPC2 F675W and ACS F658N imaging. In addition, we have deep constraints in the bluer bands F336, F435W, and F555W, which we consider in the context of a binary companion below.

[20] https://github.com/charliekilpatrick/hst123
[21] americano.dolphinsim.com/dolphot
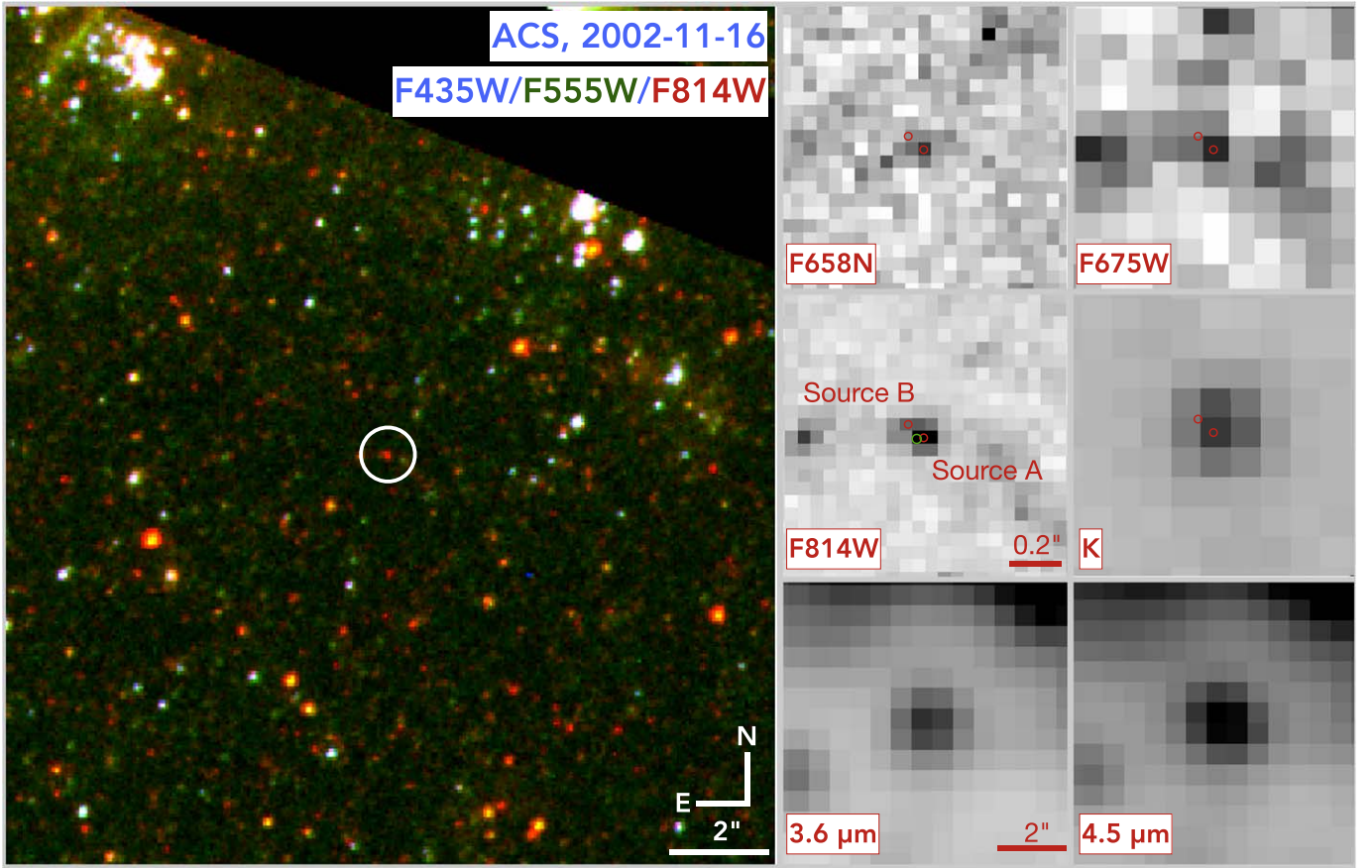
Figure 1. Left: a $15\rlap{.}''4 \times 13\rlap{.}''1$ cutout of HST/ACS imaging toward M101 in F435W (blue), F555W (green), and F814W (red). We show the approximate explosion site of SN 2023ixf as a $1''$ diameter white circle. Right panels: panels showing preexplosion F658N, F675W, F658N, Gemini/NIRI K band, and Spitzer Channel 1 (3.6 μm) and 2 (4.5 μm) imaging where we detect a counterpart at the site of SN 2023ixf. The HST and K-band images are on the same scale, while the Spitzer 3.6 and 4.5 μm images show a zoomed-out scale to highlight the location of the counterpart. We show red circles corresponding to the locations of Sources A and B, close to the site of SN 2023ixf as discussed in Section 2.1. We also note the position of the SN (with the approximate systematic uncertainty $0\rlap{.}''04$) with a green circle in the F814W panel (see Section 3.1).

Within $0\rlap{.}''2$ of the reported position of SN 2023ixf, there are two sources detected in F814W. This is clearly seen in Figure 1 where a counterpart is located at the site of SN 2023ixf in the ACS imaging and appears as a blended source in the F814W panel. The brighter source has $m_{\mathrm{F814W}} = 24.881 \pm 0.059$ mag[22] that we refer to as "Source A" (we note that this is the same source identified in Pledger & Shara 2023) and is blended with the fainter "Source B" approximately $0\rlap{.}''1$ (2.0 ACS/WFC pixels) to the northeast with $m_{\mathrm{F814W}} = 25.955 \pm 0.125$ mag. Below we consider which, if either, of these sources may be the preexplosion counterpart to SN 2023ixf and the extent to which any blended emission from other sources may contaminate the photometry of that source in other bands with poorer resolution.

2.2. Spitzer Space Telescope/IRAC

The site of SN 2023ixf was observed over 31 epochs with the Spitzer Space Telescope Infrared Array Camera (Spitzer/ IRAC) from 2004 March 8 to 2019 October 25, roughly 19.2 to 3.6 yr prior to discovery. We obtained all such imaging for the cold and warm Spitzer mission from the Spitzer Heritage Archive.[23] Following methods described in Fox et al. (2021)

and Rubin et al. (2021), we applied a forward-modeling approach to estimate the Channel 1 and 2 (3.6 and 4.5 μm, respectively) fluxes of point-like emission near the site of SN 2023ixf. After stacking and mosaicking the individual epochs in MOPEX (Makovoz & Khan 2005), we identified a single point source within $2''$ of the site of SN 2023ixf, originally reported in Szalai & van Dyk (2023) and Mayya (2023) and detected in all Channel 1 and 2 frames. We estimated the total flux of this source in the individual basic calibrated data (cbcd) frames across each epoch using realistic point-spread functions (PSFs) for the warm Spitzer mission and a python-based forward-modeling code.[24] This photometry is given in Table 2. We also provide the average photometry, which we use in our modeling below with added uncertainties accounting for the individual error bars and standard deviation across all epochs.

To validate our Spitzer photometry, we used our photometry code to analyze a sequence of 8–10 stars across every image. We looked for variability that may arise from instrumental effects or the position of the spacecraft at the time of observation. Our photometry indicates that all stars exhibit very little variability (i.e., at the <5% level) compared with the photometry of the SN 2023ixf counterpart across each epoch.

Table 2
Spitzer/IRAC Photometry of the SN 2023ixf Progenitor Candidate

MJD	Band	Flux (μJy)	Uncertainty (μJy)
53072.0903	Ch1	29.80	2.22
53072.0903	Ch2	28.97	2.74
53072.0903	Ch3	<26.78	...
53072.0903	Ch4	<30.60	...
53072.4901	Ch1	29.01	2.88
53072.4901	Ch2	26.55	3.41
53072.4901	Ch3	<27.00	...
53072.4901	Ch4	<30.72	...
55960.7226	Ch1	17.82	2.50
55980.9934	Ch1	17.50	2.44
56165.0117	Ch2	17.85	2.53
56337.0654	Ch1	16.96	2.77
56348.1056	Ch1	19.52	2.48
56516.3523	Ch2	19.01	2.55
56742.8361	Ch1	29.45	2.30
56742.8361	Ch2	32.09	1.97
56771.8253	Ch1	29.94	2.31
56771.8253	Ch2	31.37	1.75
56902.0136	Ch1	24.27	3.31
56902.0136	Ch2	26.52	3.24
57136.6924	Ch1	17.71	2.20
57136.6924	Ch2	22.66	1.83
57144.0597	Ch1	19.24	2.01
57144.0597	Ch2	20.47	1.86
57150.1719	Ch1	21.23	1.92
57150.1719	Ch2	19.67	1.72
57163.7124	Ch1	21.37	1.77
57163.7124	Ch2	25.15	1.51
57191.8234	Ch1	14.30	2.36
57191.8234	Ch2	19.11	2.03
57220.7940	Ch1	15.19	2.69
57220.7940	Ch2	18.19	2.32
57247.8227	Ch1	15.53	2.88
57247.8227	Ch2	14.94	2.37
57486.8506	Ch1	21.44	2.18
57486.8506	Ch2	24.44	1.64
57843.9334	Ch1	27.66	2.27
57843.9334	Ch2	30.23	2.00
57926.9005	Ch2	26.65	1.98
58009.6705	Ch1	22.82	2.73
58009.6705	Ch2	20.87	2.66
58232.9534	Ch1	21.63	2.13
58232.9534	Ch2	20.51	1.98
58292.8692	Ch1	17.46	1.37
58292.8692	Ch2	21.34	1.68
58380.2202	Ch1	18.29	2.84
58380.2202	Ch2	17.32	2.53
58572.0773	Ch1	22.39	2.54
58572.0773	Ch2	26.20	2.03
58614.3896	Ch1	22.33	2.44
58614.3896	Ch2	27.38	1.85
58655.6803	Ch1	25.47	2.06
58655.6803	Ch2	28.60	1.81
58697.4982	Ch1	28.49	2.53
58697.4982	Ch2	27.30	2.07
58740.0119	Ch1	22.42	3.17
58740.0119	Ch2	23.75	2.62
58781.3131	Ch1	28.26	3.17
58781.3131	Ch2	32.80	2.41
Average Spitzer/IRAC Photometry			
...	Ch1	22.13	4.78
...	Ch2	23.99	4.87

Table 2
(Continued)

MJD	Band	Flux (μJy)	Uncertainty (μJy)
...	Ch3	<21.64	...
...	Ch4	<24.15	...

Note. See Section 2.2.

(This table is available in machine-readable form.)

We conclude that variations in the counterpart are intrinsic to that source as opposed to systematic effects.

In addition, there were two epochs of Channel 3 and 4 (5.4 and 8.0 μm, respectively) data obtained at the site of SN 2023ixf from the cold Spitzer mission. We do not detect any significant source of emission in either epoch and instead place a forced circular aperture with a size of 3″0 and 3″4, or approximately 2× the FWHM of the Spitzer point-response function, at the site of SN 2023ixf. From these data, we estimate a 3σ upper limit on the presence of any emission, which is given for both epochs in Table 2. We also estimate a flux-weighted average and standard deviation of all Channel 1 and 2 photometry as well as limiting fluxes for the stacked Channel 3 and 4 imaging obtained using the same method as the individual epochs, which are all given as the last four rows in Table 2.

Finally, we consider the possibility that the Spitzer counterpart is a blend of Sources A and B, or other sources not visible in the HST bands. If all sources have similar optical–IR colors, then deblending Sources A and B in the Spitzer frames could reduce the flux of the true counterpart by 27%, comparable in magnitude to our error bars on the average values. Additional follow-up observations with JWST at late times would resolve any emission at the scale of the Source A and B separation, enabling a cleaner subtraction of any blended emission. For the analysis below, we assume that the Spitzer flux is entirely dominated by the SN 2023ixf counterpart.

2.3. Ground-based IR Imaging

The NEWFIRM IR camera (Autry et al. 2003) observed M101 in the JHK_s bands from 2010 June 29 to July 1. We obtained these data as reduced and sky-subtracted image frames from the NOIRLab data archive.[25] Stacking the frames for each band in swarp (Bertin 2010) using flux scaling derived from the calibration in their image headers, we recalibrated the final coadded image using DoPhot PSF photometry (Schechter et al. 1993) and Two Micron All Sky Survey (2MASS) JHK_s photometric calibrators in the same image frame as the NEWFIRM images (Skrutskie et al. 2006). We detect a point-like counterpart within 2″ of the site of SN 2023ixf in the K_s image, which is also the deepest NEWFIRM image overall. In summary, we find that this source has $m_{K_s} = 20.74 \pm 0.15$ mag, $m_H > 20.36$ mag, and $m_J > 20.18$ mag.

The site of SN 2023ixf was also observed by the Gemini-North telescope with the Near-Infrared Imager (NIRI) on 2010 April 18 using the K-band continuum filter and 51×50 s exposures. We processed all such imaging using pyraf-based methods from the Gemini IRAF library (Cooke &

25 https://astroarchive.noirlab.edu/

Rodgers 2005) developed for NIRI, including dark-frame subtraction, flat-fielding, sky subtraction, and optimal alignment and image coadding. We performed photometry following the same methods described above for the NEWFIRM imaging, however there were only two 2MASS K_s standard stars in the NIRI image. Therefore, we use photometry of all objects other than the SN 2023ixf counterpart that are classified as bright point sources (Object type 1) by DoPhot from the calibrated NEWFIRM K_s image to calibrate the NIRI image. Similar to the NEWFIRM imaging, there is a single point-like source within 2″ of the SN 2023ixf position, shown in Figure 1. We find that this source has $m_K = 20.72 \pm 0.08$ mag.

2.4. GMOS Imaging of SN 2023ixf

Gemini-North/GMOS obtained a series of 10×1 s images and 3×60 s images in the *gri* bands on 2023 June 3 and 5. We obtained all such imaging from the Gemini Data Archive,[26] and following standard procedures in astropy, we removed the bias from these frames using the overscan correction. We then calibrated each frame using DoPhot photometry (Schechter et al. 1993) and Pan-STARRS standard stars in each frame of the GMOS images (Flewelling et al. 2020). To obtain the deepest possible image of the field surrounding SN 2023ixf without saturating the SN position, we masked saturated pixels from the SN and stacked all images in swarp (Bertin 2010) into a single $g+r+i$ frame, weighting the individual frames by the inverse variance of the sky pixels across the individual bands. The final image centered on the position of SN 2023ixf is shown in Figure 2.

3. The Progenitor Candidate of SN 2023ifx

3.1. Aligning Pre- and Postexplosion Imaging

To establish that SN 2023ixf is associated with a candidate counterpart in preexplosion imaging, we align our postexplosion GMOS image to the ACS F814W frame and determine astrometrically whether the SN is consistent with coming from any point-like sources. Although this method can rule out an association between the SN and any preexplosion counterpart, high-resolution follow-up imaging after the SN has faded is needed to establish that any counterpart has disappeared and the association was not a chance coincidence.

We identify 108 common sources between the ACS F814W frame and Gemini $g+r+i$ image frame, which we use to establish a coordinate transformation using the IRAF package ccmap. The rms offset from this coordinate transformation solution is 0″02 in both R.A. and decl. To determine the systematic uncertainty in our coordinate transformation (and following methods from Kilpatrick et al. 2021), we take half of the astrometric calibrator sources from our sample and recalculate the coordinate transformation. We then estimate the offsets between the remaining stars. Repeating this process 100 times, we find that the average offset between stars across all trials is $\sim$0″03. In total, we estimate a 0″04 uncertainty (1.3 pc at the distance of M101) in our alignment between the two frames.

The position of SN 2023ixf aligns with Source A (Figure 2) to within 0.8σ, while it is 2.4σ away from Source B. Thus while SN 2023ixf could be astrometrically consistent with either source, there is a strong preference for Source A in our

---
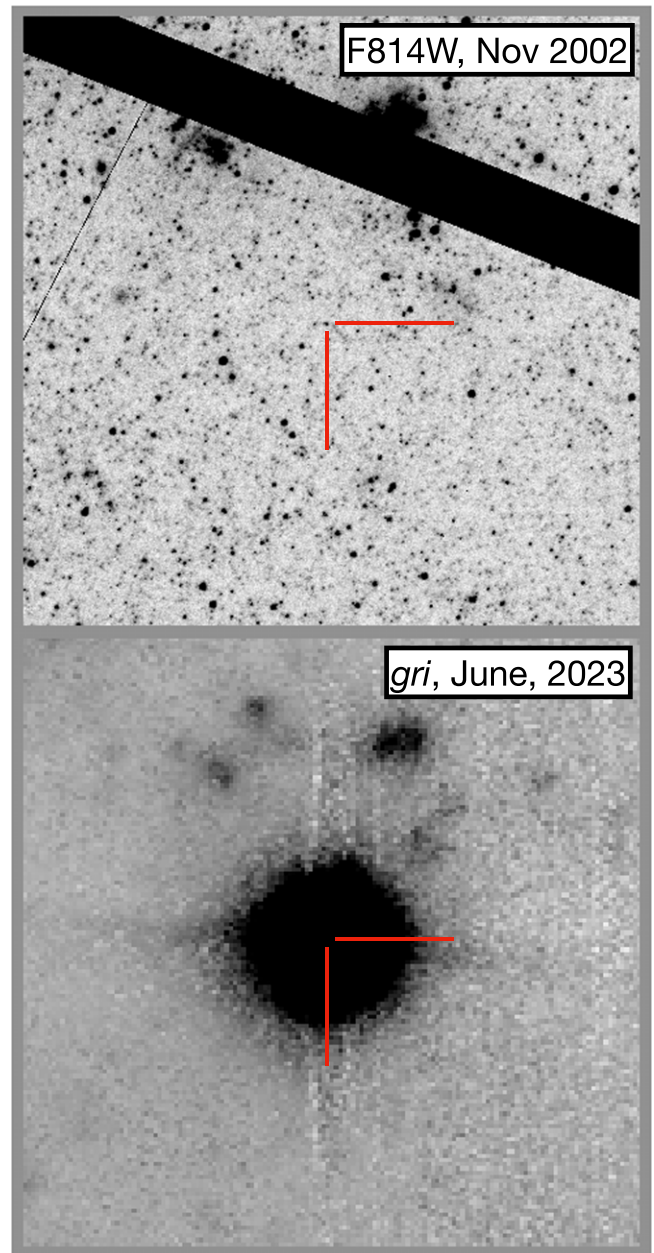
Figure 2. A part of HST/ACS F814W imaging (top) of M101 from 2002 November 16 compared with a *gri* image from Gemini-North/GMOS (bottom) of the same field from 2023 June showing the location of SN 2023ixf. We identify a single counterpart at the position of SN 2023ixf in the ACS image, discussed in detail in Section 3.1.

analysis. There is no evidence for a second source in any other image frame that we analyze, and both SN 2023ixf and Source A are astrometrically consistent with being the same object as the point sources we identified in WFPC2/F675W, ACS/F658N, Gemini/NIRI K band, and Spitzer Channels 1 and 2 across all epochs. We provide all photometry of that source in Tables 1 and 2.[27]

Finally, we estimate the probability of chance coincidence with Source A by noting that there are 238 sources detected at $>3\sigma$ within 3″ (100 pc at the distance of M101) of that source.
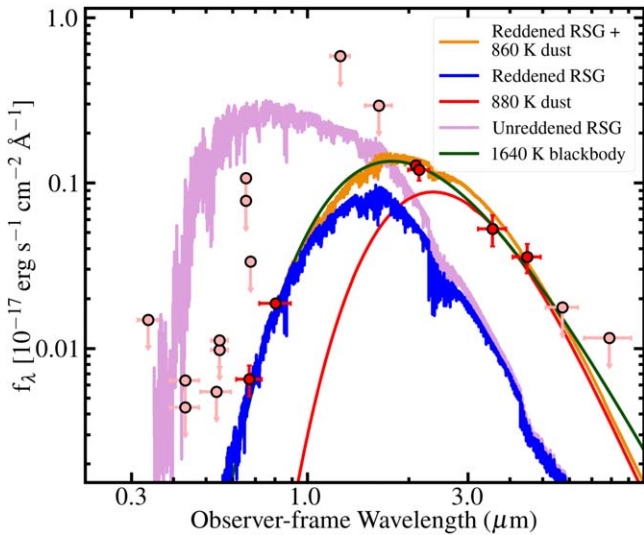
Figure 3. SED of the preexplosion counterpart to SN 2023ixf, with red circles denoting detections and pink circles denoting upper limits (described in Section 3.2). We fit the HST, Spitzer, and ground-based photometry with a 1640 K blackbody (green), which describes the data but is much cooler than typical effective temperatures for the RSG progenitor stars of SNe II (e.g., Smartt 2015). We also show an RSG SED for a reddened RSG supergiant with a $T_{\rm eff} = 3920$ K photosphere inside of a 880 K dust shell exhibiting mid-IR excess (orange; from Kilpatrick & Foley 2018) as well as the intrinsic stellar SED without reddening. The individual components of the overall reddened RSG SED (reddened star, dust shell, and unreddened star) are shown in blue, red, and purple, respectively. The SED of the preexplosion counterpart to SN 2023ixf is available as data behind the figure.

(The data used to create this figure are available.)

Therefore, there is a 4% chance of a single source landing within 1σ of the astrometric uncertainty of SN 2023ixf by chance. While this is a moderately large probability of chance coincidence, the likelihood could be reduced significantly with high-resolution follow-up imaging and, eventually, by determining whether the candidate counterpart has disappeared with follow-up observations after SN 2023ixf fades.

3.2. The SED of the SN 2023ixf Progenitor System

3.2.1. Single Blackbody Fit

Assuming that the SN 2023ixf preexplosion counterpart is dominated by a single SED from its progenitor star and with no variability between each epoch (though see the Spitzer analysis in Section 3.3), we can model the nature of this source from the ultraviolet to mid-IR. We initially adopt a simple blackbody spectrum and derive its temperature and luminosity using a Markov Chain Monte Carlo (MCMC) approach in the `python`-based package `emcee`. Assuming the distance, Milky Way extinction, and host extinction given above, we derive the in-band magnitudes for a blackbody spectrum of a given temperature and luminosity using the filter transmission functions for each space- and ground-based bandpass and using `pysynphot`. Following methods in Kilpatrick et al. (2021), we fit a blackbody model by sampling the posterior distribution over the range of model parameters, and report their posterior means and standard deviations.

Following this method, we find that the SN 2023ixf progenitor candidate is consistent with a $\log(L/L_\odot) = 4.73^{+0.07}_{-0.08}$ and $T_{\rm eff} = 1640 \pm 20$ K blackbody as

shown in Figure 3. This implied photospheric temperature is extremely low, even for the latest M supergiant spectral types (i.e., the coolest RSGs have $T_{\rm eff} = 3400$–3500 K; Levesque et al. 2006; Davies et al. 2013; Davies & Beasor 2018). The photospheric radius implied by $T_{\rm eff} = 1640$ K ($\approx 2900\,R_\odot$) suggests that we are seeing material extended well beyond the envelope of an RSG such as a shell of CSM in the local environment around the SN 2023ixf progenitor star. We infer that the photosphere in the IR is dominated by a component of host dust, and instead turn to a multicomponent SED fit below.

3.2.2. MARCS RSG and Circumstellar Dust Fit

To fit the counterpart with a more realistic optical to mid-IR SED, we use a combined RSG and dusty CSM spectrum initially presented in Kilpatrick & Foley (2018) and based on `DUSTY` radiative transfer models (from Kochanek et al. 2012; see also Ivezic & Elitzur 1997; Ivezic et al. 1999; Elitzur & Ivezić 2001). This model uses a MARCS RSG spectrum of an arbitrary temperature and luminosity (see Gustafsson et al. 2008 for details), which is reprocessed through a shell of graphitic dust at a given temperature and mass (i.e., similar to carbon-bearing species around massive RSGs; e.g., Royer et al. 2010). In general, we fit for the RSG luminosity, stellar temperature, dust temperature, and V-band optical depth through the mass of dust. These assumptions yield a mass, luminosity, and radius for the dust assuming an r^{-2} density profile (see Kochanek et al. 2012; Kilpatrick & Foley 2018 for more details). Assuming a dust-to-gas ratio and wind speed, we can then derive the total mass of CSM and mass-loss rate, which we give below.

From this model, we find that the effective temperature of the counterpart is more in line with known RSGs at $T_{\rm eff} = 3920^{+200}_{-160}$ K while the overall luminosity remains the same at $\log(L/L_\odot) = 4.74 \pm 0.07$. In order to fit the IR excess observed in the Spitzer bands, we require a circumstellar shell of dust with a V-band optical depth of $\tau_V = 5.8 \pm 0.2$ (corresponding to $A_V = 4.6 \pm 0.2$ mag) and an effective temperature of $T_{\rm dust} = 880 \pm 40$ K. This shell would have an effective radius of $8600^{+900}_{-800}\,R_\odot$ and a total dust mass of $5.0^{+1.1}_{-0.8} \times 10^{-7}\,M_\odot$, or a total mass of $5 \times 10^{-5}\,M_\odot$ assuming a dust-to-gas ratio of 0.01 in the circumstellar environment (consistent with ratios in the environments of SNe from Fox et al. 2010).

Assuming it was being produced by a constant wind with an r^{-2} profile with a velocity of $v_{\rm wind}$, the implied mass-loss rate is $\dot{M}/(v_{\rm wind}) = 1.3 \pm 0.1 \times 10^{-6}\,M_\odot\,{\rm yr}^{-1}/(50\,{\rm km\,s^{-1}})$. We assume a velocity of $50\,{\rm km\,s^{-1}}$ for consistency with W. V. Jacobson-Galán et al. (2023, in preparation), noting that this value is similar to other RSGs (e.g., 30–50 km s^{-1} for VY CMa or NML Cyg; Knapp et al. 1982; Decin et al. 2006), however high-resolution spectroscopy of unshocked material from early in the evolution of SN 2023ixf can more precisely constrain this value.

In the fits above, we do not include the ACS F658N detection despite it being spatially coincident with Source A, as this counterpart is likely dominated by Hα emission that we do not include in our model. However, assuming that the emission in this filter contains Hα and continuum emission from an RSG, we estimate that the total Hα flux density is $1.3 \times 10^{-19}\,{\rm erg\,s^{-1}\,cm^{-2}\,\mathring{A}^{-1}}$ (corrected for host and Milky Way extinction). This corresponds to a total Hα luminosity of $4.9 \times 10^{39}\,{\rm erg\,s^{-1}}$ or $1300\,L_\odot$. This value far exceeds the
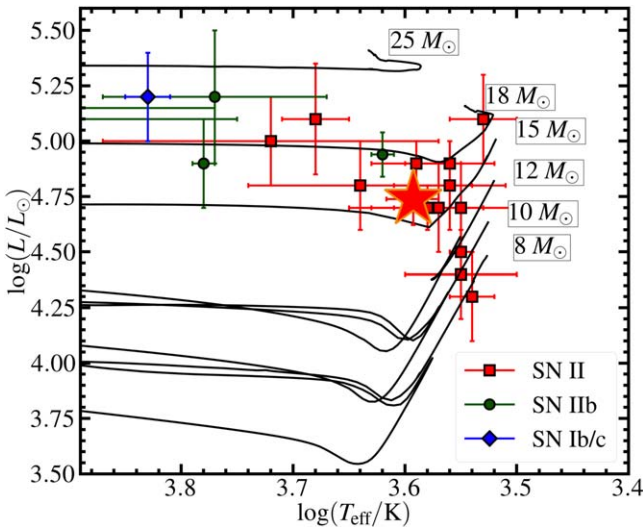
Figure 4. A Hertzsprung–Russell diagram zoomed in on the RSG branch. The location of the SN 2023ixf progenitor candidate inferred from our RSG spectral model (Section 3.2) is shown as a red star. For context, we show the locations of other SN II progenitor stars from Smartt (2015) as red squares, the progenitor stars of the SNe IIb 1993J (Aldering et al. 1994), 2011dh (Maund et al. 2011), and 2013df (Van Dyk et al. 2014) as green circles, and the progenitor candidate of the SN Ib 2019yvr (Kilpatrick et al. 2021) as a blue diamond. The black lines are single-star evolutionary tracks from MIST (Choi et al. 2016) as described in Section 3.2.

expectations for Hα emission in massive RSGs (e.g., $1\,L_\odot$ for VY CMa in Smith et al. 2001), and so may be unassociated with the progenitor star.

RSG binaries such as VV Cephei exhibit high Hα luminosities due to mass transfer from the RSG to an early-type binary companion (Wright 1977). The extreme variability in this line suggests a change in the mass transfer rate that is correlated with the properties of the wide binary orbit for this system. However, for VV Cephei, the equivalent width of ≈ 7–25 Å during the most active phases of this source implies a luminosity of $L_{H\alpha} \approx 10$–$50\,L_\odot$ (Pollmann 2005). We cannot rule out a wide binary with our optical HST limits (Section 3.2.3), which could also explain the Hα detection for an even more extreme mass transfer rate.

Assuming that the underlying star implied by our RSG model is a single source with $\log(L/L_\odot) = 4.74 \pm 0.07$, we consider its initial mass by comparing to MIST (Choi et al. 2016), STARS (Eldridge & Tout 2004), Geneva (Ekström et al. 2012), and KEPLER (Woosley & Heger 2007) models. We show the derived luminosity in comparison to the MIST models in Figure 4. All models assume solar metallicity, and either a rotating or nonrotating star. In general, the final luminosity of a model SN progenitor depends on the He core luminosity, which is higher in models including rotation and overshooting. For a MIST model assuming a star at solar metallicity, we find an initial mass of $11 \pm 1\,M_\odot$. The STARS models indicate $M_{\rm ZAMS} = 11 \pm 1\,M_\odot$, while the the Geneva rotating models produce a star of similar final luminosity at $M_{\rm ZAMS} = 11$–$12\,M_\odot$. Finally, the KEPLER (nonrotating) models indicate $M_{\rm ZAMS} = 12 \pm 1$. Thus the star could feasibly come from a system ranging from 10–13 $M_\odot$. Second dredge-up in 6–9 $M_\odot$ stars can increase the final luminosity substantially (e.g., Eldridge et al. 2007; Jones et al. 2013), with the stars along the asymptotic giant branch (AGB) ending up more luminous and with cooler photospheric temperatures

than their more massive M-type counterparts. While our DUSTY SED models favor a higher $T_{\rm eff}$ than those of AGB stars (typically $T_{\rm eff} \sim 3100$ K) it is possible the progenitor is a cooler AGB-type star. Measurements of the nickel mass created in the explosion and the oxygen mass ejected (both after 100–200 days) will provide interesting constraints on the core mass and explosion mechanism.

Finally, we examine the consistency of our derived mass-loss rate and initial mass with prescriptions from Beasor et al. (2020). Applying their luminosity-dependent mass-loss rates, we find that for RSGs of $\log(L/L_\odot) = 4.74$ they predict $\dot{M} = 0.7$–$4.2 \times 10^{-6}\,M_\odot\,{\rm yr}^{-1}$,[28] which is in close agreement with our inferred value. Similarly, applying their initial mass (for 10–12 $M_\odot$) and luminosity-dependent parameterization,[29] we derive 0.4–$1.1 \times 10^{-6}\,M_\odot\,{\rm yr}^{-1}$. These values are close to our derived mass-loss rate of $1.3 \times 10^{-6}\,M_\odot\,{\rm yr}^{-1}$, especially considering the model-dependent nature of these relations, the uncertain wind velocity, and the uncertainties in the model fitting parameters.

3.2.3. Constraints on a Binary Companion from Optical Limits

We also consider the possibility that the progenitor star evolved in a binary and exploded as the primary star in that system. Comparing our photometry to BPASS v2.2.1 binary star models (Eldridge et al. 2017), we examine all systems for which the combined flux from the primary and secondary at the time the primary explodes is fainter than our limiting magnitudes. We emphasize that these models do not include circumstellar extinction or predictions for the mid-IR luminosity, and we only use the limits from our bluer bands where we predict the primary star to be faint in order to constrain the presence of a companion star.

Although we examine all bands contained in the BPASS models for which we have deep limits (F336W, F435W, and F555W), our most constraining limit comes from ACS F555W with $m_{\rm F555W} > 27.1$ mag, corresponding to $M_{\rm F555W} > -2.2$ mag with no additional extinction from the CSM. This could be the case for a companion at wide separations with minimal additional extinction. For BPASS models with solar metallicity, this limit excludes any systems with a secondary star with $>6.4\,M_\odot$. In scenarios where the V-band circumstellar extinction ($A_V = 4.4$ mag, implying $M_{\rm F555W} > -6.6$ mag) is taken into account, virtually all BPASS models are consistent with our limits. A close binary therefore remains a possibility for SN 2023ixf, whose presence could better be constrained with deep optical imaging after the SN fades.

3.3. Preexplosion Variability of the Progenitor Candidate and Implications for Mass Loss

The SN 2023ixf progenitor star exhibited extreme variability in the Spitzer/IRAC bands several years before explosion (Figure 5). We show the light curve of the counterpart at 3.6 and 4.5 μm from ∼2012–2020 in Figure 5. For comparison, we also show the 3.9 μm light curve of α Orionis (Betelgeuse) from 2017 January 1 to 2022 December 12 (Taniguchi et al. 2022), but shifted in time by 4 yr so it overlaps with that of the SN 2023ixf counterpart and scaled to its average flux at ∼23 μJy. In the SED analysis above, we emphasize that we

---

[28] See Equation (3) and Table 4 in Beasor et al. (2020).
[29] See Equation (4) in Beasor et al. (2020).
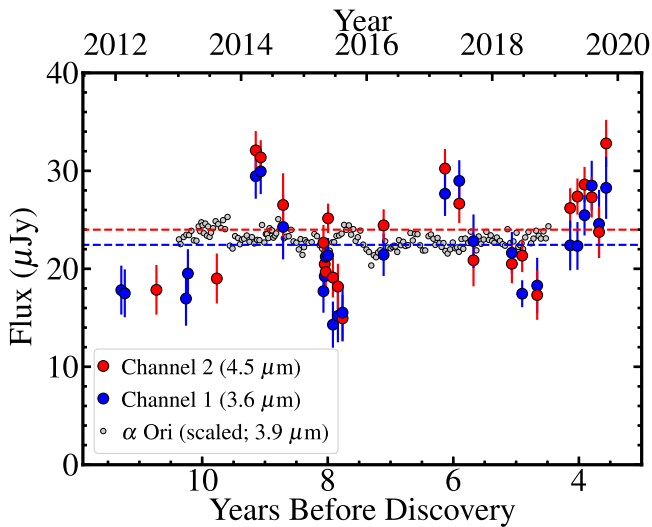
Figure 5. Light curve of the preexplosion counterpart to SN 2023ixf from Spitzer/IRAC Channel 1 and 2 observations from ∼11.3–3.6 yr prior to discovery of the SN. We note that both channels exhibit ∼16 μJy peak-to-peak variability during this time frame, with a significant peaks spaced ∼2.8 yr apart. The flux-weighted average in Channels 1 and 2 are shown as blue and red dashed lines, respectively, with their values given in Table 2. For comparison, we show the 3.9 μm light curve of Betelgeuse binned every 2 weeks from Taniguchi et al. (2022), scaled to the average flux of the SN 2023ixf counterpart at ∼23 μJy and shifted in time by 4 yr to overlap with our light curve.

accounted for intrinsic variations in the Spitzer bands by including the standard deviation across the light curves in the average Channel 1 and 2 fluxes.

The SN 2023ixf progenitor star exhibited significant mid-IR variability with an average of 22.44 and 23.99 μJy and peak-to-peak variability of 15.64 and 17.86 μJy at 3.6 and 4.5 μm, respectively (roughly 0.8 mag or 70% in both bands). These extreme variations appear correlated in the two Spitzer bands with approximately the same overall magnitude, which would be consistent with a mode of variability where the visible photosphere expands and contracts with at most small variations in effective temperature. We also note that these variations are similar in amplitude to the high-luminosity end of large-amplitude, cool pulsators observed in the LMC (O'Grady et al. 2020, 2023).

Moreover, the light curve from 2012–2020 exhibits as quasi-sinusoidal variation with a timescale of roughly 2.8 yr (1000 day). We infer this timescale via a Fourier transform of the Spitzer/IRAC photometry, although the sampling of the light curve and the fact that we only observe peak-to-peak variations over ∼2.5 cycles in Figure 5 suggests it is uncertain and could vary anywhere from 2.6–3.0 yr. Combined, this evidence is similar to the κ-mechanism pulsations in Betelgeuse, which are the primary mode of variability in that star and are driven by changes in the atmospheric opacity (see, e.g., Li & Gong 1994; Heger et al. 1997). Paxton et al. (2013) observe these modes with timescales of 1–8 yr directly in MESA models of RSGs where the structure of the star is resolved with sufficiently high time resolution, also in close agreement with the simulations in Yoon & Cantiello (2010) and our inferred timescale. These pulsations drive expansion and contraction in the atmosphere at a nearly constant temperature (e.g., Levesque & Massey 2020), resulting in overall changes to the luminosity from Betelgeuse.

In addition, the significant variability correlated across both bands supports the conclusion that the Spitzer counterpart is dominated by a single source. As this variability is extreme in the IR even for a single RSG, the flux is unlikely to contain significant emission from a second source (e.g., Source B) compared with the minimum flux level of our light curve in Figure 5.

Assuming this mechanism is responsible for the variability in the SN 2023ixf counterpart, the required changes in luminosity are ≈50% larger than in Betelgeuse. Our derived mass-loss rate is comparable with Betelgeuse (which has a rate from 0.2–2 × $10^{-6} M_\odot \, \text{yr}^{-1}$; Dolan et al. 2016), which matches expectations for the κ-mechanism driving strong mass loss with large variations in luminosity. However, our estimate precludes a "superwind" generated in the CSM (e.g., Yoon & Cantiello 2010; Davies et al. 2022) up to the point where our data cut off 3.6 yr before explosion. The preexplosion mass-loss rate could be enhanced if the star was significantly more active during the final 3 yr before core collapse, which is predicted by W. V. Jacobson-Galán et al. (2023, in preparation).

4. Discussion

Current estimates of the maximum luminosity of SN II progenitor stars are dominated by a handful of direct counterpart detections in the literature (e.g., Davies & Beasor 2018; Kochanek 2020), and the highest-luminosity stars in those samples contribute significant weight to statistical analyses of the distribution from which they are drawn.

Assuming the SN 2023ixf candidate counterpart is dominated by its progenitor star emission in the HST, Spitzer, and ground-based imaging, SN 2023ixf provides the best example to date of the optical to mid-IR SED of an SN II progenitor star (comparable to SN 2017eaw; Kilpatrick & Foley 2018; Rui et al. 2019; Van Dyk et al. 2019), but with a low foreground host-galaxy extinction and precise distance. The significant variability and large implied circumstellar extinction support the presence of such features in other SN II progenitor stars given the lack of multiepoch, multiband imaging in which they can be analyzed. The vast majority of directly detected SN II progenitor stars in recent analyses (Smartt 2015; Davies & Beasor 2018; Kochanek 2020) were identified from F814W imaging. Our analysis of SN 2023ixf demonstrate that it has extreme bolometric corrections when accounting for its mid-IR luminosity. This has been explored in the past as a possible explanation to the RSG problem (Walmswell & Eldridge 2012), but our dust mass estimates imply a much larger extinction than has been previously explored for SN II progenitor stars. However even with the significant stellar flux in the near- and mid-IR, the total preexplosion luminosity indicates an initial mass significantly below 20 $M_\odot$. Future systems with Spitzer or JWST detections similar to SN 2023ixf can constrain the distribution of that extinction from their IR excess.

5. Conclusion

We have presented direct imaging showing that there is a credible progenitor candidate to the type II SN 2023ixf in M101 at 6.85 Mpc. In summary, this imaging demonstrates:

1. The candidate progenitor star to SN 2023ixf is most consistent with a $\log(L/L_\odot) = 4.74 \pm 0.07$ RSG with an effective temperature of $T_{\text{eff}} = 3920^{+200}_{-160}$ K. Following

single-star evolutionary tracks, this would place the progenitor star's initial mass at $11 \pm 2\,M_\odot$, placing it within the range of other low- to moderate-mass RSG progenitors to SNe II (e.g., Smartt 2015).

2. Modeling of the mid-IR SED from this counterpart suggests that it was enshrouded in a dusty shell of CSM similar to SN 2017eaw (Kilpatrick & Foley 2018). The implied mass-loss rate for a wind that could produce this shell divided by its wind speed is $\dot{M}/v_{\mathrm{wind}} = 1.3 \pm 0.1 \times 10^{-6}\,M_\odot\,\mathrm{yr}^{-1}/(50\,\mathrm{km\,s}^{-1})$. This is comparable to more massive stars such as Betelgeuse but low compared to a "superwind" or mass-loss rates from immediately before explosion inferred in W. V. Jacobson-Galán et al. (2023, in preparation).

3. Spitzer/IRAC photometry exhibits significant preexplosion variability that is correlated in both bands. We also see evidence for a 2.8 yr (1000 day) timescale in this variability, similar to but generally stronger in amplitude than pulsations in other RSGs driven by opacity changes in their atmosphere (i.e., the κ mechanism; Li & Gong 1994; Heger et al. 1997; Yoon & Cantiello 2010; Paxton et al. 2013).

Future studies of the progenitor stars to SNe II will greatly benefit from multiband, multiepoch imaging of resolved stellar populations using deep optical and IR surveys of nearby galaxies, such as those by the Vera C. Rubin Observatory and Nancy Grace Roman Space Telescope (Ivezić et al. 2019; Gezari et al. 2022). To understand these stars better, their preexplosion evolution, and the exact cause of the RSG problem, only detailed SEDs and light curves from the optical to mid-IR, such as those that we present for the SN 2023ixf counterpart, can shed light on the pathways through which SN II progenitor stars evolve and explode.

Data Availability

All data and analysis products presented in this article are available upon request. Analysis code and photometry used in this paper are available on GitHub: https://github.com/charliekilpatrick/progenitors; a copy of this material has been deposited to Zenodo: 10.5281/zenodo.8060641. The HST data used in this paper can be found in MAST: 10.17909/dqc4-yx93. The Spitzer Space Telescope data used in this paper can be found in the Spitzer Heritage Archive (IRSA 2022) (AORS: 44605696, 44605952, 45237504, 48186624, 50627072, 50627328, 50627840, 52776448, 52776704, 52776960, 52777216, 52777472, 52777728, 52777984, 52778240, 60830720, 60830976, 60831232, 60831488, 60831744, 60832000, 66022400, 66022656, 66022912, 66023168, 66023424, and 66023680). Gemini data (GN-2010A-Q-27) are publicly available on the Gemini data archive at https://archive.gemini.edu/ and NEWFIRM data (Prop IDs: 2012A-0540) are from the NOIRLab Astro Data Archive at https://astroarchive.noirlab.edu/.

ORCID iDs

Charles D. Kilpatrick ⓘ https://orcid.org/0000-0002-5740-7747
Ryan J. Foley ⓘ https://orcid.org/0000-0002-2445-5275
Wynn V. Jacobson-Galán ⓘ https://orcid.org/0000-0002-3934-2644
Anthony L. Piro ⓘ https://orcid.org/0000-0001-6806-0673
Stephen J. Smartt ⓘ https://orcid.org/0000-0002-8229-1731
Maria R. Drout ⓘ https://orcid.org/0000-0001-7081-0082
Alexander Gagliano ⓘ https://orcid.org/0000-0003-4906-8447
Christa Gall ⓘ https://orcid.org/0000-0002-8526-3963
Jens Hjorth ⓘ https://orcid.org/0000-0002-4571-2306
David O. Jones ⓘ https://orcid.org/0000-0002-6230-0151
Kaisey S. Mandel ⓘ https://orcid.org/0000-0001-9846-4417
Raffaella Margutti ⓘ https://orcid.org/0000-0003-4768-7586
Enrico Ramirez-Ruiz ⓘ https://orcid.org/0000-0003-2558-3102
Conor L. Ransome ⓘ https://orcid.org/0000-0003-4175-4960

V. Ashley Villar ⓘ https://orcid.org/0000-0002-5814-4061
David A. Coulter ⓘ https://orcid.org/0000-0003-4263-2228
Hua Gao ⓘ https://orcid.org/0000-0003-1015-5367
David Jacob Matthews ⓘ https://orcid.org/0000-0002-4513-3849
Kirsty Taggart ⓘ https://orcid.org/0000-0002-5748-4558
Yossef Zenati ⓘ https://orcid.org/0000-0002-0632-8897

References

Adams, S. M., Kochanek, C. S., Gerke, J. R., Stanek, K. Z., & Dai, X. 2017, MNRAS, 468, 4968
Aldering, G., Humphreys, R. M., & Richmond, M. 1994, AJ, 107, 662
Arnett, W. D., Bahcall, J. N., Kirshner, R. P., & Woosley, S. E. 1989, ARA&A, 27, 629
Astropy Collaboration, Price-Whelan, A. M., Lim, P. L., et al. 2022, ApJ, 935, 167
Autry, R. G., Probst, R. G., Starr, B. M., et al. 2003, Proc. SPIE, 4841, 525
Beasor, E. R., Davies, B., Smith, N., et al. 2020, MNRAS, 492, 5994
Bertin E. (2010) SWarp: Resampling and Co-adding FITS Images Together, Astrophysics Source Code Libraryascl:1010.068
Brown, T. M., Baliber, N., Bianco, F. B., et al. 2013, PASP, 125, 1031
Byrne, R. A., & Fraser, M. 2022, MNRAS, 514, 1188
Choi, J., Dotter, A., Conroy, C., et al. 2016, ApJ, 823, 102
Cooke, A., & Rodgers, B. 2005, in ASP Conf. Ser. 347, Astronomical Data Analysis Software and Systems XIV, ed. P. Shopbell, M. Britton, & R. Ebert (San Francisco, CA: ASP), 514
Coulter, D. A., Jones, D. O., McGill, P., et al. 2022, YSE-PZ: An Open-source Target and Observation Management System, v0.3.0, Zenodo, doi:10.5281/zenodo.7278430
Coulter, D. A., Jones, D. O., McGill, P., et al. 2023, PASP, 135, 064501
Crockett, R. M., Smartt, S. J., Pastorello, A., et al. 2011, MNRAS, 410, 2767
Davies, B., & Beasor, E. R. 2018, MNRAS, 474, 2116
Davies, B., Kudritzki, R.-P., Plez, B., et al. 2013, ApJ, 767, 3
Davies, B., Plez, B., & Petrault, M. 2022, MNRAS, 517, 1483
Decin, L., Hony, S., de Koter, A., et al. 2006, A&A, 456, 549
Dolan, M. M., Mathews, G. J., Lam, D. D., et al. 2016, ApJ, 819, 7
Dolphin A. (2016) DOLPHOT: Stellar photometry, Astrophysics Source Code Libraryascl:1608.013
Drout, M. R., Massey, P., & Meynet, G. 2012, ApJ, 750, 97
Ekström, S., Georgy, C., Eggenberger, P., et al. 2012, A&A, 537, A146
Eldridge, J. J., Mattila, S., & Smartt, S. J. 2007, MNRAS, 376, L52
Eldridge, J. J., Stanway, E. R., Xiao, L., et al. 2017, PASA, 34, e058
Eldridge, J. J., & Tout, C. A. 2004, MNRAS, 353, 87
Elias-Rosa, N., Van Dyk, S. D., Li, W., et al. 2010, ApJL, 714, L254
Elitzur, M., & Ivezić, Ž 2001, MNRAS, 327, 403
Fernández, R., Quataert, E., Kashiyama, K., & Coughlin, E. R. 2018, MNRAS, 476, 2366
Flewelling, H. A., Magnier, E. A., Chambers, K. C., et al. 2020, ApJS, 251, 7
Foreman-Mackey, D., Hogg, D. W., Lang, D., & Goodman, J. 2013, PASP, 125, 306
Fox, O. D., Chevalier, R. A., Dwek, E., et al. 2010, ApJ, 725, 1768
Fox, O. D., Khandrika, H., Rubin, D., et al. 2021, MNRAS, 506, 4199
Fraser, M., Ergon, M., Eldridge, J. J., et al. 2011, MNRAS, 417, 1417
Fraser, M., Maund, J. R., Smartt, S. J., et al. 2014, MNRAS, 439, L56
Fraser, M., Takáts, K., Pastorello, A., et al. 2010, ApJL, 714, L280
Fuller, J. 2017, MNRAS, 470, 1642
Gal-Yam, A., Arcavi, I., Ofek, E. O., et al. 2014, Natur, 509, 471
Gal-Yam, A., & Leonard, D. C. 2009, Natur, 458, 865
Gezari, S., Bentz, M., De, K., et al. 2022, arXiv:2202.12311
Guo, J. H., & Li, Y. 2002, ApJ, 565, 559
Gustafsson, B., Edvardsson, B., Eriksson, K., et al. 2008, A&A, 486, 951
Hack, W. J., Cara, M., Sosey, M., et al. 2021, spacetelescope/drizzlepac: Drizzlepac v3.3.0, v3.3.0, Zenodo, doi:10.5281/zenodo.5534751
Heger, A., Jeannin, L., Langer, N., & Baraffe, I. 1997, A&A, 327, 224
Hillebrandt, W., Hoeflich, P., Weiss, A., & Truran, J. W. 1987, Natur, 327, 597
IRSA 2022, Spitzer Heritage Archive, IPAC, [Data set], doi:10.26131/IRSA543
Itagaki, K. 2023, TNSTR, 2023-1158, 1
Ivezic, Z., & Elitzur, M. 1997, MNRAS, 287, 799
Ivezic, Z., Nenkova, M., & Elitzur, M. 1999, arXiv:astro-ph/9910475
Jacobson-Galán, W. V., Dessart, L., Jones, D. O., et al. 2022, ApJ, 924, 15
Jones, S., Hirschi, R., Nomoto, K., et al. 2013, ApJ, 772, 150
Jurcevic, J. S., Pierce, M. J., & Jacoby, G. H. 2000, MNRAS, 313, 868

Ivezić, Ž, Kahn, S. M., Tyson, J. A., et al. 2019, ApJ, 873, 111
Khazov, D., Yaron, O., Gal-Yam, A., et al. 2016, ApJ, 818, 3
Kilpatrick, C. D. 2021, charliekilpatrick/hst123: hst123, v1.0.0, Zenodo, doi:10.5281/zenodo.5573941
Kilpatrick, C. D. 2023, charliekilpatrick/progenitors: progenitors, v1.0.0, Zenodo, doi:10.5281/zenodo.8060641
Kilpatrick, C. D., Drout, M. R., Auchettl, K., et al. 2021, MNRAS, 504, 2073
Kilpatrick, C. D., & Foley, R. J. 2018, MNRAS, 481, 2536
Kilpatrick, C. D., Fong, W.-f., Blanchard, P. K., et al. 2022, ApJ, 926, 49
Kilpatrick, C. D., & Rubin, D. 2023, charliekilpatrick/forwardmodel: forwardmodel, v1.0.0, Zenodo, doi:10.5281/zenodo.8060639
Knapp, G. R., Phillips, T. G., Leighton, R. B., et al. 1982, ApJ, 252, 616
Kochanek, C. S. 2020, MNRAS, 493, 4945
Kochanek, C. S., Khan, R., & Dai, X. 2012, ApJ, 759, 20
Kochanek, C. S., Shappee, B. J., Stanek, K. Z., et al. 2017, PASP, 129, 104502
Levesque, E. M., & Massey, P. 2020, ApJL, 891, L37
Levesque, E. M., Massey, P., Olsen, K. A. G., et al. 2006, ApJ, 645, 1102
Li, Y., & Gong, Z. G. 1994, A&A, 289, 449
Lovegrove, E., & Woosley, S. E. 2013, ApJ, 769, 109
Makovoz, D., & Khan, I. 2005, in ASP Conf. Ser. 347, Astronomical Data Analysis Software and Systems XIV, ed. P. Shopbell, M. Britton, & R. Ebert (San Francisco, CA: ASP), 81
Maund, J. R., Fraser, M., Ergon, M., et al. 2011, ApJL, 739, L37
Maund, J. R., Fraser, M., Smartt, S. J., et al. 2013, MNRAS, 431, L102
Maund, J. R., Mattila, S., Ramirez-Ruiz, E., & Eldridge, J. J. 2014, MNRAS, 438, 1577
Maund, J. R., & Smartt, S. J. 2009, Sci, 324, 486
Mayya, D. 2023, TNSAN, 147, 1
Morozova, V., Piro, A. L., & Valenti, S. 2017, ApJ, 838, 28
Morozova, V., Piro, A. L., & Valenti, S. 2018, ApJ, 858, 15
Müller, T., Prieto, J. L., Pejcha, O., & Clocchiatti, A. 2017, ApJ, 841, 127
Neugent, K. F. 2021a, ApJ, 908, 87
Neugent, K. F. 2021b, ApJ, 908, 87
Neugent, K. F., Levesque, E. M., Massey, P., Morrell, N. I., & Drout, M. R. 2020, ApJ, 900, 118
Neustadt, J. M. M., Kochanek, C. S., Stanek, K. Z., et al. 2021a, MNRAS, 508, 516
Neustadt, J. M. M., Kochanek, C. S., Stanek, K. Z., et al. 2021b, MNRAS, 508, 516
O'Grady, A. J. G., Drout, M. R., Gaensler, B. M., et al. 2023, ApJ, 943, 18
O'Grady, A. J. G., Drout, M. R., Shappee, B. J., et al. 2020, ApJ, 901, 135
O'Neill, D., Kotak, R., Fraser, M., et al. 2019, A&A, 622, L1

Paxton, B., Cantiello, M., Arras, P., et al. 2013, ApJS, 208, 4
Piro, A. L. 2013, ApJL, 768, L14
Pledger, J. L., & Shara, M. M. 2023, arXiv:2305.14447
Pollmann, E. 2005, PAICz, 93, 44
Riess, A. G., Yuan, W., Macri, L. M., et al. 2022, ApJL, 934, L7
Royer, P., Decin, L., Wesson, R., et al. 2010, A&A, 518, L145
Rubin, D., Cikota, A., Aldering, G., et al. 2021, PASP, 133, 064001
Rui, L., Wang, X., Mo, J., et al. 2019, MNRAS, 485, 1990
Schechter, P. L., Mateo, M., & Saha, A. 1993, PASP, 105, 1342
Schlafly, E. F., & Finkbeiner, D. P. 2011, ApJ, 737, 103
Science Software Branch at STScI (2012) PyRAF: Python alternative for IRAF, Astrophysics Source Code Libraryascl:1207.011
Skrutskie, M. F., Cutri, R. M., Stiening, R., et al. 2006, AJ, 131, 1163
Smartt, S. J. 2009, ARA&A, 47, 63
Smartt, S. J. 2015, PASA, 32, e016
Smartt, S. J., Eldridge, J. J., Crockett, R. M., & Maund, J. R. 2009, MNRAS, 395, 1409
Smartt, S. J., Maund, J. R., Hendry, M. A., et al. 2004, Sci, 303, 499
Smith, N., Humphreys, R. M., Davidson, K., et al. 2001, AJ, 121, 1111
Sollerman, J., Yang, S., Schulze, S., et al. 2021, A&A, 655, A105
Soraisam, M. D., Bildsten, L., Drout, M. R., et al. 2018, ApJ, 859, 73
Stothers, R. 1969, ApJ, 156, 541
Sukhbold, T., Ertl, T., Woosley, S. E., Brown, J. M., & Janka, H.-T. 2016, ApJ, 821, 38
Szalai, T., & van Dyk, S. 2023, ATel, 16042, 1
Taniguchi, D., Yamazaki, K., & Uno, S. 2022, NatAs, 6, 930
Terreran, G., Jacobson-Galán, W. V., Groh, J. H., et al. 2022, ApJ, 926, 20
Tinyanont, S., Ridden-Harper, R., Foley, R. J., et al. 2022, MNRAS, 512, 2777
Tody, D. 1986, Proc. SPIE, 627, 733
Tomasella, L., Cappellaro, E., Fraser, M., et al. 2013, MNRAS, 434, 1636
Van Dyk, S. D., Bostroem, K. A., Andrews, J. E., et al. 2023b, MNRAS, Advance Access
Van Dyk, S. D., de Graw, A., Baer-Way, R., et al. 2023a, MNRAS, 519, 471
Van Dyk, S. D., Zheng, W., Fox, O. D., et al. 2014, AJ, 147, 37
Van Dyk, S. D., Zheng, W., Maund, J. R., et al. 2019, ApJ, 875, 136
Walmswell, J. J., & Eldridge, J. J. 2012, MNRAS, 419, 2054
Woosley, S. E., & Heger, A. 2007, PhR, 442, 269
Wright, K. O. 1977, JRASC, 71, 152
Yang, M., & Jiang, B. W. 2011, ApJ, 727, 53
Yaron, O., Perley, D. A., Gal-Yam, A., et al. 2017, NatPh, 13, 510
Yoon, S.-C., & Cantiello, M. 2010, ApJL, 717, L62